
USING A MODIFIED DOUBLE DEEP IMAGE PRIOR FOR CROSSTALK MITIGATION IN MULTISLICE PTYCHOGRAPHY

Ming Du

Advanced Photon Source
Argonne National Laboratory
Lemont, Illinois 60439, USA
mingdu@anl.gov

Xiaojing Huang

National Synchrotron Light Source II
Brookhaven National Laboratory
Upton, New York 11973, USA

Chris Jacobsen

Advanced Photon Source
Argonne National Laboratory, Lemont, Illinois 60439, USA
{Department of Physics & Astronomy, Chemistry of Life Processes Institute}
Northwestern University
Evanston, Illinois 60208, USA
cjacobsen@anl.gov

Abstract

Multislice ptychography is a high-resolution microscopy technique used to image multiple separate axial planes using a single illumination direction. However, multislice ptychography reconstructions are often degraded by crosstalk, where some features on one plane erroneously contribute to the reconstructed image of another plane. Here, we demonstrate the use of a modified “double deep image prior” (DDIP) architecture in mitigating crosstalk artifacts in multislice ptychography. Utilizing the tendency of generative neural networks to produce natural images, a modified DDIP method yielded good results on experimental data. For one of the datasets, we show that using DDIP could remove the need of using additional experimental data, such as from x-ray fluorescence, to suppress the crosstalk. Our method may help x-ray multislice ptychography work for more general experimental scenarios.

1 Introduction

In ptychography, a spatially-limited coherent probe is scanned across multiple transverse positions; the collection of far-field diffraction patterns are then used to reconstruct the complex optical transmittance of a planar object [1]. Multislice ptychography [2, 3] is an extension of this approach for imaging multiple axial planes each separated by a distance z_{DoF} greater than the depth of field (DoF) of [4, 5]

$$z_{\text{DoF}} = \frac{2}{0.61^2} \frac{\delta_t^2}{\lambda} \simeq 5.4 \frac{\delta_t^2}{\lambda} \quad (1)$$

where δ_t is the transverse spatial resolution. In multislice ptychography, the probe illumination function at each probe position is modulated by the first axial plane, after which Fresnel propagation is used to bring it to the next plane, and so on until the far-field diffraction intensity is obtained.

When the contrast of upstream planes is significant enough that the first Born approximation is violated, the illumination of downstream planes is significantly affected; if incorrectly accounted for in a reconstruction algorithm, this can lead to crosstalk between the images from these separate planes. Even with low contrast objects, if the axial separation between object planes is only a small multiple of z_{DoF} , Fresnel propagation alone may be insufficient to cleanly reconstruct the two planes correctly. This can be seen in a 12 keV x-ray multislice ptychography experiment where crosstalk was observed in $\delta_t = 9.2$ nm images of objects on two planes separated by 10 μm , or 2.3 times $z_{\text{DoF}} = 4.4$ μm in this case [6]. Given that hard x-ray microscopy is well suited to imaging objects in this thickness range [7], this limitation of

multislice ptychography becomes important to overcome. Alternative approaches include ptychographic tomography for objects that do not extend in depth beyond z_{DoF} at any rotation angle [8], or multislice ptychographic tomography of thicker objects where propagation is used to compensate for Fresnel diffraction blurring but images of separate planes are not required [9, 10, 11, 5, 12]; however, both of these approaches require images obtained over multiple object rotation angles. The more extensive data collection required for these tomographic approaches is not always feasible or desirable, so it remains important to overcome crosstalk effects in single-viewing-direction multislice ptychography of separate object planes.

Many ptychographic beamlines at synchrotron light sources are equipped with both an area detector for recording far-field coherent diffraction data, and an energy-dispersive detector for recording x-ray fluorescence (XRF) signals in the same scan of the illumination probe. Unlike ptychography, fluorescence imaging is an incoherent process with a spatial resolution limited by the focusing optic used; however, XRF can provide low spatial frequency information of a sample with distinct distributions of chemical elements. This approach has been used to provide low-crosstalk reconstructions of an upstream plane object consisting of an Au zone plate structure and a downstream plane consisting of NiO particles mounted on a silicon nitride window [13]. In this case, the Ni XRF image was used to generate an initial guess of the object on the downstream plane, as well as to subtract the spectrum of the NiO object’s “ghost image” from an initial reconstruction of the upstream plane, after which a multislice ptychographic reconstruction was allowed to proceed. The resulting images (shown in Figs. 3(a) and (b) of [13]) indeed show almost no crosstalk between the reconstructed images at the two axial planes.

While the XRF-aided reconstruction has been shown to be effective, its limitation is also apparent: if the chemical composition of objects on the different axial planes is similar, then XRF can no longer provide strict object separation. Therefore, it is valuable to explore alternative methods to suppress crosstalk without using XRF data. In fact, the crosstalk separation problem resembles the well-known problem of blind source separation (BSS) problem in signal processing [14]. In the BSS problem, one begins with N measurement $\mathbf{y} = [y_1(t), y_2(t), \dots, y_N(t)]$, where each measurement is a linear superimposition of M source signals $\mathbf{s} = [s_1(t), s_2(t), \dots, s_M(t)]$ with a unique set of weighting factors $w_{n,m}$ so that one obtains measured data of $y_n(t) = \sum_m^M w_{n,m} s_m(t)$. The goal in this case is to solve the linear system

$$\mathbf{y} = \mathbf{A}\mathbf{s} \quad (2)$$

so as to obtain the source signals \mathbf{s} . The problem can be overdetermined, underdetermined, or exactly determined depending on the relative values of M and N . Separating out all M sources requires $N \geq M$. Obviously, for multislice ptychography, $N = M$, which is a necessary condition for all “clean” slices to be solved from phase retrieved slices containing crosstalk.

The complication for multislice ptychography is that the ghost features are not a simple superimposition added onto an affected slice, but rather a filtered version of the real features after losing information in certain spatial frequency bands. For example, the ghost particles in one axial plane of Fig. 4(a) of [6] appear like a low-pass filtered version of features in the other axial plane. This band loss has to be taken into account before separating the ghost features. Moreover, for a BSS problem to be solved successfully, the rows of \mathbf{A} in Eq. 2 should be linearly independent. In the case of multislice ptychography, that requires sufficient differentiation between real and ghost features in the axial slices. When the slice spacing is large, this condition is usually easy to satisfy. However, if the slice separation is too small, the weak probe variation between adjacent slices makes them hard to be cleanly reconstructed when starting from a random guess, since this can yield retrieved slices that are too similar to each other. Under this scenario, we may relax our constraint and allow the use of XRF data to assist with the initial phase retrieval. However, it turns out that even with good initial guesses aided by XRF, one is still unable to fully eliminate inter-slice crosstalk without very a careful search of reconstruction parameters and reconstruction algorithms. For example, to obtain Fig. 3(a) and (b) of [13], many efforts were made to optimize the algorithm and parameters. Before doing that, a standard reconstruction yielded images with considerable crosstalk as shown in Fig. 4(a) of [13] and as will be shown again below. We demonstrate here that crosstalk can be greatly reduced, so that in both situations (large separation without using XRF, and small separation with XRF), the crosstalk can be mitigated using a neural network algorithm based on a “double deep image prior”, or “double-DIP” (DDIP).

In the deep image prior (DIP) approach [15], images in the forward model are generated from a generative neural network, so that the network itself functions to provide prior knowledge to the system. This is because a deep neural network prefers generating “natural images” with lower patch-wise entropy, rather than those with higher patch-wise entropy [16]. In fact, the DIP is a type of “untrained” neural network, which means that instead of using a large dataset to train a DIP, one uses the original image in a specific image reconstruction task, and uses the trained DIP only for this task itself. As such, a shallow network suffices for a DIP since it only needs to “learn” from the image(s) being processed, and the generalizability of a DIP-based algorithm is not constrained by the training set. This initial demonstration of DIP [15] used an encoder–decoder structure which learns to map an input tensor to an image with the same spatial dimension. By using an encoder–decoder network with skip connections linking the encoder part and the

decoder part, one can lead the network to generate images with structure at multiple spatial scales, thus better capturing the characteristics of natural images.

Building upon this initial work, it has been shown that the use of multiple DIP networks can achieve improved outcomes on a series of layer decomposition problems including image dehazing, image segmentation, and transparency separation whose goal is to separate out multiple individual natural images from blends of them [16]. All these tasks can be carried out using a similar architecture: if there are two layers to be separated, one can use two DIP networks to generate two distinct images, and use a third DIP to generate either a mask or a constant blending ratio. The architecture is thus named “double-DIP” (DDIP) after the two image-generating DIPs. Using the generated images and the mask or ratio, one can synthesize a blended image, and train the networks to minimize a loss function measuring the mismatch between the synthesized image and the original blended images. The preference of DIPs to generate natural images means that the local patches consisting the images they generate usually have lower empirical entropy, which is an indication that these images are more likely to be unblended “single” images. Additionally, prior work [16] also included an exclusion term in the loss function, which penalizes the correlation between the spatial gradients of the generated images. This further suppresses the crosstalk in the output images.

Therefore, one can expect that the DDIP architecture can function effectively in the multislice ptychography crosstalk separation problem. In view of the additional band loss complication of the ghost features, we modified the DDIP architecture from the original design of [16]. The network architecture will be introduced in more detail in Section 2. In Section 3, we will show the results obtained using DDIP on two datasets, each representing one of the slice spacing situations mentioned above.

2 Methods

2.1 Algorithm

The overall model structure of our modified DDIP is shown in Fig. 1. The two image-generating DIPs, labeled DIP-1 and DIP-2, are of the same “U-Net”-like architecture [17], as shown in Fig. 2. The kernel size used in all 2D convolutional layers is 5×5 ; an exception is the skip connections, where 1×1 kernels are used. The input/output numbers of channels of these convolutional layers are shown in the figure. A leaky ReLU is used after each 2D convolutional layer as the activation function. The inputs to both DIPs, z_1 and z_2 , are mono-channel tensors of random numbers that are uniformly sampled between -0.5 and 0.5 and have the same height and width as the original images. The DIP that generates the constant weighting factor, DIP-3, adopts the same architecture as DIP-1 and 2 except that the input and output numbers of channels are 2. During training, DIP-1 and 2 learn to map z_1 and z_2 to y_1 and y_2 which are supposed to be the “clean” slice images. For DIP-3, the values of the central pixels from both output channels are used as the blending weights α_1 and α_2 . In [16], a linear combination is used to synthesize the blended images I_1 and I_2 from generated images y_1 and y_2 , *i.e.*, $I_1 = \alpha_1 y_1 + (1 - \alpha_1) y_2$, and $I_2 = \alpha_2 y_1 + (1 - \alpha_2) y_2$. In our case, to account for the band loss of the ghost features, we pass the images of the source of crosstalk through an additional function f_1 or f_2 , giving

$$\begin{aligned} I_1 &= \alpha_1 y_1 + (1 - \alpha_1) f_1(y_2) \\ I_2 &= \alpha_2 f_2(y_1) + (1 - \alpha_2) y_2. \end{aligned} \quad (3)$$

We explored two types of choices for f_1 and f_2 . Before discussing the choices for these functions, one can see in Fig. 3(a) and 4(a) that the ghost images from more strongly scattering materials (*e.g.*, gold) appear like the high-pass filtered version of the real features. On the other hand, the more weakly scattering materials (*e.g.*, NiO) contribute to the crosstalk with a low-passed version of the real features. Thus, one can define f_1 and f_2 as two single-kernel filtering functions, which can be implemented through 2D convolution:

$$\begin{aligned} f_1(x) &= x * k_1 \\ f_2(x) &= x * k_2. \end{aligned} \quad (4)$$

Based on the appearance of the original images, k_1 and k_2 can be initialized to be a low-pass or high-pass kernel. During training, their values are optimized along with the DIP parameters. For our results to be shown in Section 3 where both cases are consisted of one slice with low-pass crosstalk and another with high-pass crosstalk, we set k_1 to be a 7×7 uniform filter, and k_2 to be a 7×7 kernel containing a 5-point Laplacian filter.

Using a single filtering kernel may not be able to capture the band loss at various spatial scales. Therefore, a second way is to set f_1 and f_2 as another two shallow DIPs with downsampling and skip connections. In our implementation, we used a 3-layer DIP with the same kernel size as DIP-1, 2, and 3, so that there are 3 downsampling/upsampling operations, each with a factor of 2. However, the number of channels of intermediate tensors is always 1. Additionally,

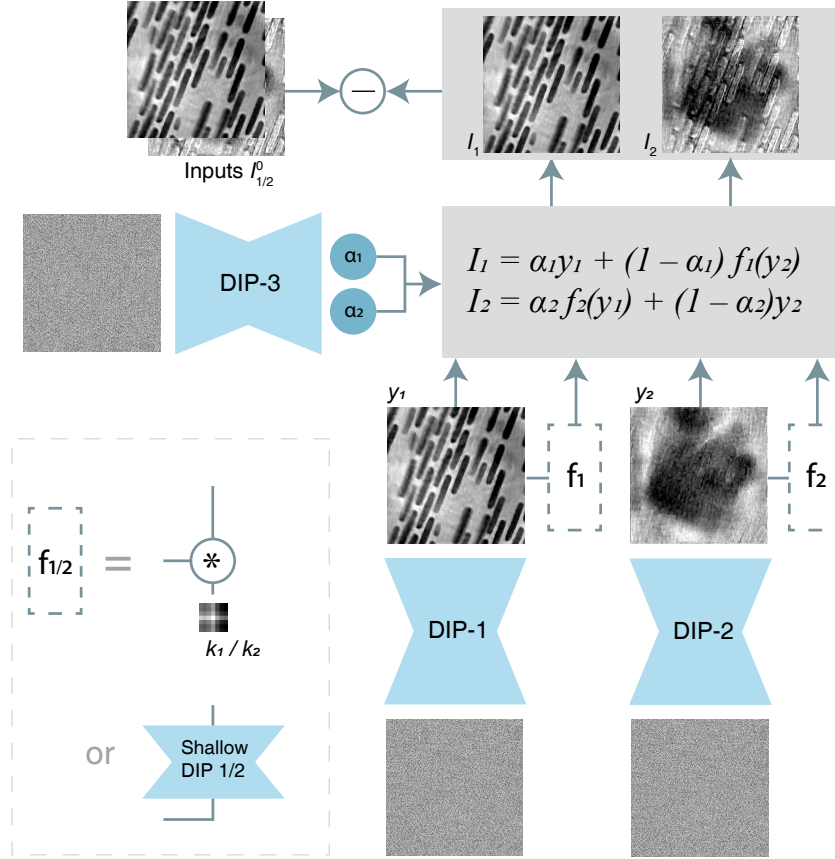


Figure 1: The ‘‘double DIP’’ model used in this work. Following prior work[16], the outputs of both image-generating deep image priors (DIPs; as shown in Fig. 2) are filtered by function $f_{1/2}$ to account for the partial band transfer of superimposed images. $f_{1/2}$ can be either a single-layer filter, or a shallow DIP network.

skip connections are used at all 3 spatial scales in order to prevent the loss of high-frequency information. These shallow DIPs are initialized using uniform random numbers, and the parameters are optimized along with the ‘‘major’’ DIPs during training.

With these, we can now formulate the loss function which contains a data mismatch term measuring the difference between the synthesized images $I_{1/2}$ and the original images, $I_{1/2}^0$. Additionally, as indicated in [16], it is also essential to employ an exclusion loss which penalizes the correlation of the spatial gradients of y_1 and y_2 at multiple spatial scales. The values of α_1 and α_2 are also penalized for drifting away from 0.5 at the first 100 epochs of the algorithm in order to stabilize their values against the random input and network initialization. Thus, the full loss function (for a 2-slice separation task) is written as

$$L = \sum_{i=1}^2 \|I_i(\text{DIP-1,2,3}, f_{1,2}) - I_i^0\|^2 + \gamma_{\text{excl}} \sum_{j=1}^5 \sum_{l \in \{x,y\}} D_j(\nabla_l y_1) D_j(\nabla_l y_2) + \chi_{[1,100]}(k) \sum_{i=1}^2 \|\alpha_i - 0.5\|^2 \quad (5)$$

where γ_{excl} is a constant weight of the exclusion loss term, D_j is the downsampling function that downsamples the image in its argument by a factor of 2^{j-1} , $\nabla_l y$ denotes the spatial gradient of y along direction l (either x or y), and $\chi_{[1,100]}(k)$ is a step function of epoch number k that returns 1 when $k \leq 100$, and 0 otherwise.

Our model is trained on an HP Z8 G4 workstation with two Intel Xeon Silver 4108 CPUs and two NVIDIA Quadro P4000 GPUs, although the model is run using only one GPU each time. PyTorch [18] is used for automatic differentiation. The code is available on <https://github.com/mdw771/ddip4ptycho>.

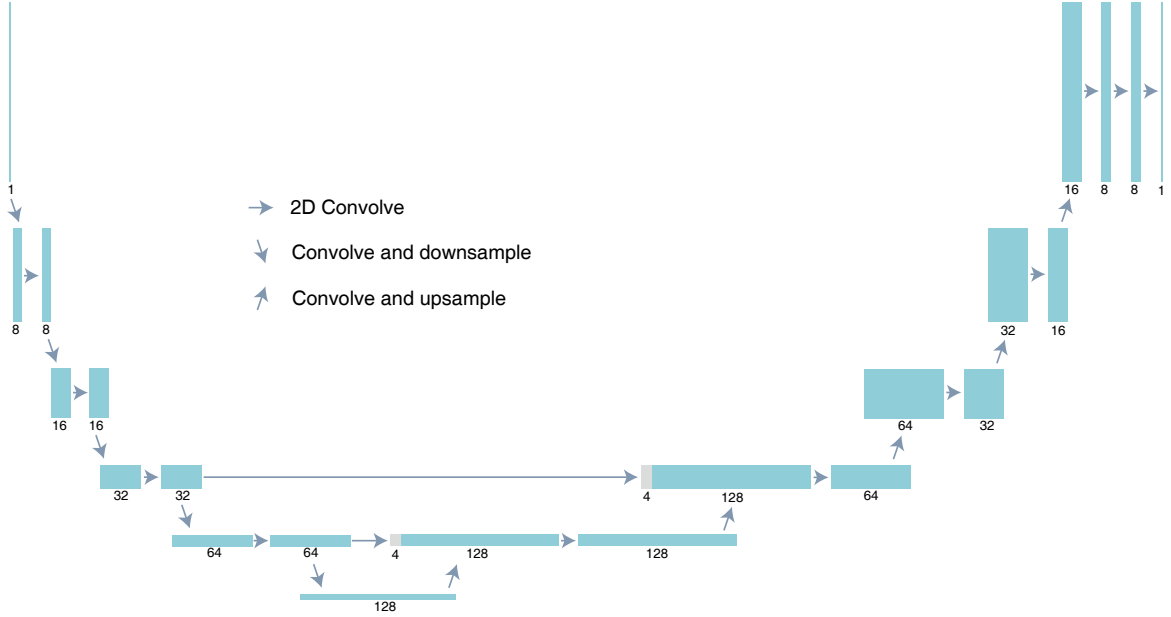


Figure 2: Architecture of a DIP network used in the DDIP model. Numbers underneath tensor blocks indicate the number of channels.

2.2 Beamline experiments

The datasets used in both cases shown in Section 3 were acquired at the Hard X-ray Nanoprobe beamline (3-ID) of the National Synchrotron Light Source II at Brookhaven National Laboratory.

The first dataset involves a synthetic sample, where Au nanoparticles and NiO particles are deposited on both sides of a 10- μm -thick Si wafer. We will hereafter refer to this dataset as the Au/NiO dataset. The dataset was collected with a beam energy of 12 keV and a transverse resolution $\delta_t = 7.3$ nm, which, according to Eq. 1 gives $z_{\text{DoF}} = 2.8$ μm . The 10- μm slice spacing is therefore about 3.6 times larger than z_{DoF} . The multislice reconstruction result of this dataset was published earlier in [6], which can be referred for more experimental details. Similar to [6], we assume two slices in the sample, which respectively correspond to the Au layer and the NiO layer.

The second dataset, described here as the ZP/NiO dataset, also involves a 2-slice sample that has been previously published [13]. In this case, Au zone plate structures and NiO particles are deposited on both sides of a 500-nm-thick silicon nitride membrane. The beam energy and transverse resolution on the first slice are 12 keV and 8.7 nm, giving $z_{\text{DoF}} = 3.9$ μm . Hence, the slice spacing is just about 0.13 of the DoF.

3 Results

3.1 Large-spacing separation for Au/NiO data

The crosstalk-contaminated slice images of the Au/NiO dataset were reconstructed using an adaptive momentum based algorithm in a tool we developed called “Adorym” [19]. The phase retrieval was initialized using Gaussian randoms, without using the XRF data. Because the slice spacing is 3.6 times larger than z_{DoF} , our multislice reconstruction algorithm is able to provide reconstructions of both slices with the “true” features of each slice resolved sharply, but they also exhibit obvious ghost features due to the crosstalk. Next, we cropped a 272×272 pixel area that has full probe overlap from each slice [Fig. 3(a)], and passed the slices to DDIP as I_1^0 and I_2^0 .

We performed 5 test runs with $f_{1/2}$ set to use either shallow DIPs or single filters for $f_{1/2}$, and with different values of γ_{excl} . Each parameter combination was run for 10000 epochs. When using shallow DIPs for $f_{1/2}$, the peak GPU memory usage was 439 MB, and each run took around 30 min to complete. The results are shown in Fig. 3(b-f), where the final values of α_1 and α_2 are indicated at the top right corners of the corresponding subplots as $\alpha_1|\alpha_2$. The dynamic range of all plots is set to $[\mu - 4\sigma, \mu + 4\sigma]$, with μ and σ being the image mean and standard deviation.

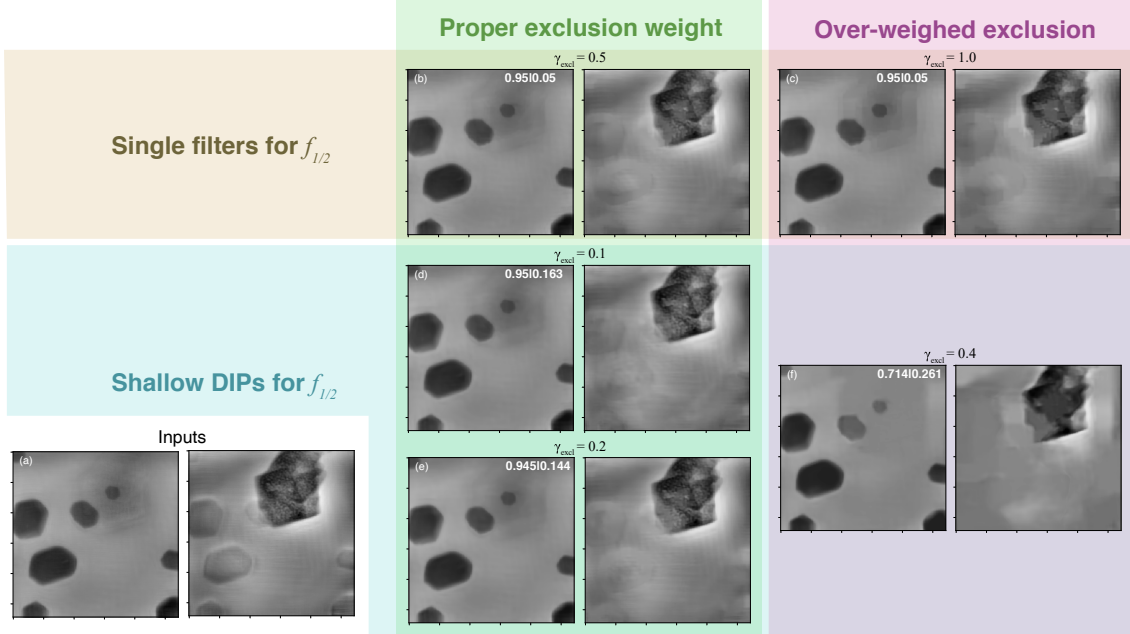


Figure 3: Input images (a) and separation results (b-f) of the Au/NiO dataset. The results were obtained with $f_{1/2}$ set to either single filters or shallow DIPs. For each case, several γ_{excl} values were tested. Ghost features are effectively suppressed with a proper setting for γ_{excl} . However, when γ_{excl} is too large, fine details of the features are smeared out. The final values of $\alpha_1|\alpha_2$ are indicated at the upper right corners of the corresponding subplots. The values of α hold steady except when we use shallow DIPs for $f_{1/2}$ and over-weight the exclusion loss, in which case the ratio α_1/α_2 decreases significantly.

Since the ghost image on slice 1 of the NiO particle (which is in fact on slice 2) is very blurry, it appears like a subtle change in the image background. Under all tested parameter settings, DDIP barely affected the presence of this faint region. This can be explained by the nature of deep image priors: as noted in [16], generative neural networks tend to generate images that have a smaller empirical entropy across its local patches; in other words, the generated images tend to have “strong internal self-similarity”. Since the ghost feature on slice 1 is very smooth, it is hard for DIPs to exclude it from the generated image. However, the ghost features on slice 2 are sharp and have a much higher variance. They make the local patches of the image more complicated and more “unlike” to each other, so DIP tends to generate images that are free of these artifacts. Therefore, the improvement of slice 2 are obvious. The effect on slice 2 is also largely dependent on γ_{excl} regardless whether $f_{1/2}$ is set to use shallow DIPs or single filters. When using single filters for $f_{1/2}$, the setting of $\gamma_{excl} = 0.5$ can provide an apparent mitigation of the crosstalk coming from slice 1, where the sharpness and contrast of the ghost Au particles are greatly reduced. Increasing γ_{excl} to 1.0 suppresses the ghost features even further, but it also starts to destroy details in the “true image” of the NiO particle. In particular, the regions in the NiO particle that overlap with ghost Au particles are severely smeared. Given such high values of γ_{excl} , the correlation of gradients is over-penalized and the algorithm tends to reduce the spatial gradient of slice 2 at the overlapping regions to 0, resulting in flattened areas.

Improved results are obtained when we switch $f_{1/2}$ to use shallow DIPs. In Fig. 3(d), when $\gamma_{excl} = 0.1$, the crosstalk suppression on slice 2 is nearly as effective as (b) with single filters and $\gamma_{excl} = 0.5$. Increasing γ_{excl} to 0.2 slightly enhances the suppression effect, surpassing the efficacy of Fig. 3(c) with single filters and $\gamma_{excl} = 1.0$. Moreover, comparing (c) and (e) reveals that using shallow DIPs leads to much better preserved high-frequency details in the NiO particle. This is an expected improvement, as the multi-scale filtering with skip connections in the shallow DIPs better describes the band loss of ghost features than single filters. If one increases γ_{excl} further to 0.4, however, the images would start to lose high-frequency details as well.

The final values of blending weights for all cases are composed of a large α_1 and a small α_2 . Based on Eq. 3, this indicates that y_1 contributes much more than $f_1(y_2)$ does to I_1 , while y_2 contributes more than $f_2(y_1)$ to I_2 . This is a reasonable trend as one would expect smaller contribution from the ghost features than real features in a “blended” slice. However, we should not interpret the α values as the absolute intensities of the ghost or real features present in I_1

or I_2 , since the mean intensities of y_1 , y_2 , $f_1(y_2)$, and $f_2(y_1)$ can vary as well. On the other hand, the α pair may be used as an indication of the fidelity of the result. In Fig. 3(f) where the details of the features are obviously undermined, the final value of α_1 is much lower than other results with better preserved features, while α_2 is much higher. Since the algorithm always tries to minimize the mismatch between $I_{1/2}$ and $I_{1/2}^0$ where the latter is fixed, unusual α values point to unusual value ranges of the outputs of DIP-1/2 and $f_{1/2}$, implying that the generated images might be highly aberrated.

3.2 Small-spacing separation for ZP/NiO data

The 500-nm slice spacing in the ZP/NiO dataset is only about 0.13 times the DoF. As such, our attempt of reconstructing both slices using random initial guesses yielded two slices that are largely undifferentiated. The superimposed features on both slices are mixed with an almost identical ratio, and the band loss of ghost features is very small. Images like this could hardly provide enough diversity of measurement in order to solve the BSS problem. Therefore, it becomes essential to employ the XRF data as additional prior knowledge to the reconstruction algorithm. As mentioned earlier, the slice images to be separated were obtained using the XRF-aided method described in [13], where the XRF map of Ni is used to reduce the contrast of NiO in the single-slice reconstruction, leaving the Au zone plate structure, and the NiO-removed Au image and the re-sampled Ni XRF map are used as the initial guess for the first and second slice, respectively, for the subsequent multislice ptychographic phase retrieval. Without dedicated parameter tuning and algorithm search, standard phase retrieval could not provide well separated slices; instead, it yielded the slice images shown in Fig. 4(a), where slice 2 is heavily affected by the ghost images from the Au zone plate structures on slice 1. Our goal is to show that, even though XRF data have to be used, DDIP can provide better separated images based on this result, so that the excessive amount of phase retrieval parameter tuning may be avoided.

We again tested several γ_{excl} values with $f_{1/2}$ using shallow DIPs or single filters. 10000 epochs are run for each case. When using shallow DIPs, the peak memory usage is 1130 MB, and it took 37 min to complete the training. On the other hand, when using single filters, the total walltime becomes 31 min, though the peak memory usage did not change significantly since the parameter size of the shallow DIPs is rather small compared to the major DIPs. The results are shown in Fig. 4(b-h). Similar to what was observed with the Au/Ni dataset, the crosstalk does not significantly affect slice 1, but results in obvious ghost images on slice 2 due to the strong scattering of Au. For single filters, $\gamma_{\text{excl}} = 0.4$ [Fig. 4(c)] gives the best balance between crosstalk suppression and feature fidelity. Using a lower γ_{excl} of 0.1 leaves a lot of residual ghost image features, while a higher value of 1.0 results in a blocky appearance of the recovered slice 2. When using shallow DIPs, the optimal γ_{excl} is found around 0.1. If γ_{excl} is set too high, the fidelity of y_2 is dramatically lost, which is accompanied by a much larger α_2 .

Since the Au zone plate structures are well aligned in the same direction, we can analyze the power spectra of the outcome y_2 to evaluate the effectiveness of crosstalk suppression. These power spectra are normalized by the integrated energy, and plotted on a logarithmic scale. In the power spectra of the original image shown in Fig. 4(a), one can clearly observe a slanted streak that represents the periodicity of the zone plate ghost features. For $\gamma_{\text{excl}} = 0.4$ when using single filters and $\gamma_{\text{excl}} = 0.1$ when using shallow DIPs, the streak becomes barely visible. Further increasing γ_{excl} in both cases cause energy to concentrate in the low-frequency region, associated with the smeared appearance of (d) and (g).

4 Discussion

We have demonstrated the crosstalk separation capability of our modified DDIP model in two cases, one with slice images reconstructed without using XRF data, the other reconstructed using the aid of XRF data but without fine tuning of phase retrieval parameters. In practice, one problem of concern might be the reproducibility of the algorithm due to its inherent uncertainty, which is contributed by the randomness of input vectors z_1 , z_2 , z_3 and the random initialization of network parameters. In our experience, this uncertainty is associated with the value of γ_{excl} , so we conducted a test to evaluate the change of result distribution with γ_{excl} . On the Au/Ni dataset, we ran a series of DDIP separations using $\gamma_{\text{excl}} = 0.04, 0.1, 0.2, 0.4$, each run for 20 times. For the results of each γ_{excl} , the standard deviation over the 20 runs at each pixel position is shown in Fig. 5(a-d). The averages of these standard deviation maps are plotted in Fig. 5(e), which clearly show an increasing trend. Referring back to Fig. 3, the optimal result using shallow DIPs is obtained with $\gamma_{\text{excl}} = 0.2$, where the image mean is 0.68, but the uncertainty standard deviation is only around 0.04. In practice, one can also perform multiple runs and use the average y_1 and y_2 as the final results, so as to further decrease the uncertainty. Other than the detailed variation of the separated images, it is also possible for DDIP to undergo ‘‘slice confusion’’: since the inputs to the generating DIPs are purely random, they do not inform DDIP that y_1 should correspond to real features on slice 1, and vice versa for y_2 . If DDIP is confused about the slice arrangement, it may tend to generate the real, solid Au particles, which should lie on slice 1, on y_2 instead. According to Eq. 3, these Au particles will be filtered by f_1 to

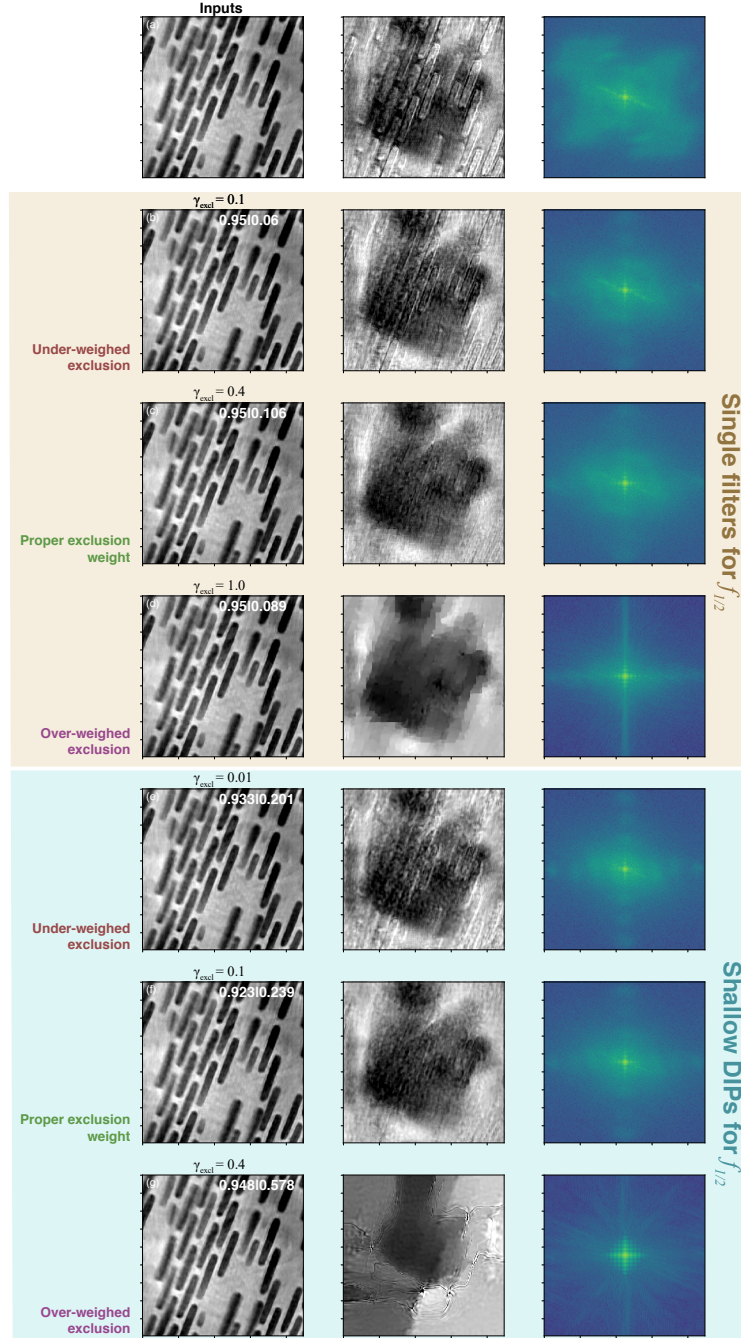


Figure 4: Input images (a) and separation results (b-g) of the ZP/NiO dataset. Like in the cases shown in Fig. 3, the results were obtained with $f_{1/2}$ set to either single filters or shallow DIPs. The final values of $\alpha_1|\alpha_2$ are indicated at the upper right corners of the corresponding subplots. While the influence of γ_{excl} on slice 1 is minimal, it greatly affects the balance between separation effectiveness and image resolution for slice 2. The rightmost column shows the normalized power spectra of slice 2. A slanted streak corresponding to the periodicity of the zone plate’s ghost features can be seen obviously in the input image’s spectrum. In the outputs of the DDIP (*i.e.*, y_2), the spectrum density of this streak becomes much lower. Also, we again see that when we use shallow DIPs for $f_{1/2}$ and over-weight the exclusion loss, a smaller α_1/α_2 ratio is yielded.

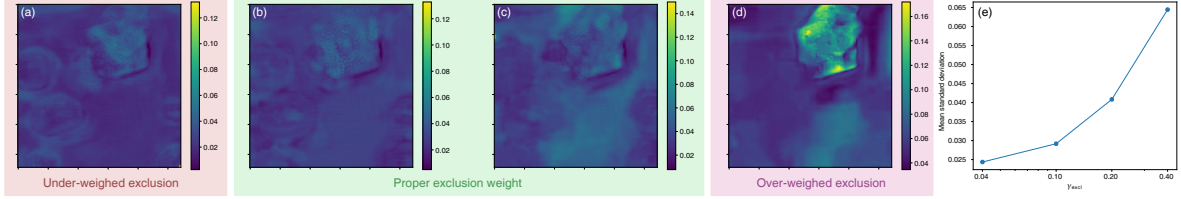


Figure 5: (a-d) Standard deviation maps of output slice 2 (y_2) of the Au/Ni dataset, calculated from 20 independent runs, for $\gamma_{\text{excl}} = 0.04, 0.1, 0.2, 0.4$. (e) plots the mean standard deviation against γ_{excl} . These standard deviation values measure the uncertainty of DDIP, as the input vectors to the DIPs are randomly initialized for each run. Larger γ_{excl} results in larger uncertainty.

form I_1 , which is unphysical; the same would apply to I_2 . However, with a reasonable γ_{excl} , this is very unlikely to happen: following the example above, if the real Au particles appear on y_2 , then they will appear unfiltered on I_2 ; yet, on I_2^0 these particles are highpass filtered, and this leads to high mismatch loss which is unfavored. Therefore, the band loss of feature blending and our unsymmetrical use of $f_{1/2}$ in the forward model drive the DDIP towards the correct slice arrangement. In our uncertainty test, we did not see slice confusion in all of our 80 separation results.

Both results shown in Section 3 involve 2 slices. In practice, multislice ptychography may be used to reconstruct 3 slices or more, and mutual crosstalk may involve more than 2 slices. In that case, one may add more DIPs, so that the number of image-generating DIPs matches the number of mutually crosstalking slices N . Meanwhile, the input and output channels of the weight-generating DIP may be increased to N , and the forward model of Eq. 3 may be expanded to N equations, constituting an $N \times N$ mixing matrix. Using too many DIPs will unavoidably impair the efficiency of the algorithm. However, in x-ray microscopy, the number of slices is typically small due to the large DoF of X rays. Making the DDIP method more efficient for many-slice problems is a future direction to explore.

5 Conclusion

Using a modified double-DIP architecture, we demonstrated the use of deep neural networks in mitigating the crosstalk artifacts of multislice ptychography phase retrieval. When the slice spacing is large (many multiples of the DoF), phase retrieval from scratch can provide slice reconstructions that are distinct from each other but affected by crosstalk, while post-processing using DDIP may suppress or remove the crosstalk on each slice. Combining multislice phase retrieval and DDIP can yield good reconstructions without XRF data in this case. When the slice spacing is small, phase retrieval may need the aid of XRF data in order to generate distinguishable slice images, and the retrieved images may still contain crosstalk artifacts without dedicated parameter tuning. One can also use DDIP in this case to suppress the crosstalk, so that one no longer has to spend time searching for the best values of phase retrieval hyperparameters. In order to account for the band loss of crosstalking features in a slice image, we pass the them through a filtering function in our forward model. The filtering function can take the form of either a single convolutional filter or a shallow DIP. While the former is faster, the latter can often provide results with better preserved details. We expect that the findings will help improve the adaptability of multislice ptychography in imaging thick samples beyond the DoF limit.

Acknowledgement

This research used resources of the Advanced Photon Source (APS), a U.S. Department of Energy (DOE) Office of Science User Facility operated for the DOE Office of Science by Argonne National Laboratory under Contract No. DE-AC02-06CH11357. It also used 3ID of the National Synchrotron Light Source II, a U.S. Department of Energy (DOE) Office of Science User Facility operated for the DOE Office of Science by Brookhaven National Laboratory under Contract No. DE-SC0012704. We thank the Argonne Laboratory Directed Research and Development for support under grant 2019-0441. We also thank the National Institute of Mental Health, National Institutes of Health, for support under grant R01 MH115265. We appreciate the authors of the “double-DIP” paper (Gandelsman *et al.* [16]) for sharing their code, which we adapted and modified for this work.

Disclosure

The authors declare no conflicts of interest.

References

- [1] H M L Faulkner and J Rodenburg. Movable aperture lensless transmission microscopy: A novel phase retrieval algorithm. *Physical Review Letters*, 93(2):023903, July 2004.
- [2] A M Maiden, M J Humphry, and J M Rodenburg. Ptychographic transmission microscopy in three dimensions using a multi-slice approach. *Journal of the Optical Society of America A*, 29(8):1606–1614, August 2012.
- [3] Esther H R Tsai, Ivan Usov, Ana Diaz, Andreas Menzel, and Manuel Guizar-Sicairos. X-ray ptychography with extended depth of field. *Optics Express*, 24(25):29089–29108, 2016.
- [4] Max Born, Emil Wolf, A. B. Bhatia, P. C. Clemmow, D. Gabor, A. R. Stokes, A. M. Taylor, P. A. Wayman, and W. L. Wilcock. *Scattering from inhomogeneous media*, pages 695–734. Cambridge University Press, 7 edition, 1999.
- [5] M A Gilles, Y S G Nashed, M Du, C Jacobsen, and S M Wild. 3D x-ray imaging of continuous objects beyond the depth of focus limit. *Optica*, 5:1078–1085, 2018.
- [6] Hande Öztürk, Hanfei Yan, Yan He, Mingyuan Ge, Zhihua Dong, Meifeng Lin, Evgeny Nazaretski, Ian K Robinson, Yong S Chu, and Xiaojing Huang. Multi-slice ptychography with large numerical aperture multilayer Laue lenses. *Optica*, 5(5):601–607, May 2018.
- [7] Ming Du and Chris Jacobsen. Relative merits and limiting factors for x-ray and electron microscopy of thick, hydrated organic materials. *Ultramicroscopy*, 184:293–309, 2018.
- [8] Martin Dierolf, Andreas Menzel, Pierre Thibault, Philipp Schneider, Cameron M Kewish, Roger Wepf, Oliver Bunk, and Franz Pfeiffer. Ptychographic x-ray computed tomography at the nanoscale. *Nature*, 467(7314):436–439, September 2010.
- [9] Wouter Van den Broek and Christoph T Koch. Method for retrieval of the three-dimensional object potential by inversion of dynamical electron scattering. *Physical Review Letters*, 109(24):245502, December 2012.
- [10] Ulugbek S Kamilov, Ioannis N Papadopoulos, Morteza H Shoreh, Alexandre Goy, Cedric Vonesch, Michael Unser, and Demetri Psaltis. Learning approach to optical tomography. *Optica*, 2(6):517–522, 2015.
- [11] Peng Li and Andrew Maiden. Multi-slice ptychographic tomography. *Scientific Reports*, 8:2049, January 2018.
- [12] Ming Du, Youssef S G Nashed, Saugat Kandel, Dogã Gürsoy, and Chris Jacobsen. Three dimensions, two microscopes, one code: automatic differentiation for x-ray nanotomography beyond the depth of focus limit. *Science Advances*, 6:eaay3700, March 2020.
- [13] Xiaojing Huang, Hanfei Yan, Yan He, Mingyuan Ge, Hande Öztürk, Yao-Lung L. Fang, Sungsoo Ha, Meifeng Lin, Ming Lu, Evgeny Nazaretski, Ian K. Robinson, and Yong S. Chu. Resolving 500 nm axial separation by multi-slice x-ray ptychography. *Acta Crystallographica Section A*, 75(2):336–341, 2019.
- [14] Xi-Ren Cao and Ruey-Wen Liu. General approach to blind source separation. *IEEE Transactions on Signal Processing*, 44(3):562–571, 1996.
- [15] Dmitry Ulyanov, Andrea Vedaldi, and Victor Lempitsky. Deep image prior. *2018 IEEE/CVF Conference on Computer Vision and Pattern Recognition*, pages 9446–9454, 2018.
- [16] Yossi Gandelsman, Assaf Shocher, and Michal Irani. “Double-DIP”: Unsupervised image decomposition via coupled deep-image-priors. arXiv:1812.00467, 2018.
- [17] Olaf Ronneberger, Philipp Fischer, and Thomas Brox. U-Net: Convolutional networks for biomedical image segmentation. arXiv:1505.04597, 2015.
- [18] Adam Paszke, Sam Gross, Francisco Massa, Adam Lerer, James Bradbury, Gregory Chanan, Trevor Killeen, Zeming Lin, Natalia Gimelshein, Luca Antiga, Alban Desmaison, Andreas Kopf, Edward Yang, Zachary DeVito, Martin Raison, Alykhan Tejani, Sasank Chilamkurthy, Benoit Steiner, Lu Fang, Junjie Bai, and Soumith Chintala. Pytorch: An imperative style, high-performance deep learning library. In H. Wallach, H. Larochelle, A. Beygelzimer, F. d’Alché-Buc, E. Fox, and R. Garnett, editors, *Advances in Neural Information Processing Systems 32*, pages 8024–8035. Curran Associates, Inc., 2019.
- [19] Ming Du, Saugat Kandel, Junjing Deng, Xiaojing Huang, Arnaud Demortiere, Tuan Tu Nguyen, Remi Tucoulou, Vincent De Andrade, Qiaoling Jin, and Chris Jacobsen. Adorym: A multi-platform generic x-ray image reconstruction framework based on automatic differentiation. arXiv:2012.12686, 2020.